Optimizing CBTSSe solar cells for indoor applications through numerical simulation

Saif M. H. Qaid[1] · **Ahmed Shaker**[2] · **Mohamed Okil**[3] · **Muath Alkadi**[4] ·
Abdullah Ahmed Ali Ahmed[5] · **Walid Zein**[2]

Abstract

Solar cell technologies are pivotal in the transition towards sustainable energy sources. This paper delves into the design and optimization of CBTSSe solar cells for efficient indoor energy harvesting. The tunable bandgap nature of CBTSSe aligns well with the emission spectra of indoor LED lighting, making it a promising candidate for such applications. Our investigations in this paper commence with the design validation of a solar cell device structure, in line with experimental work, ensuring the accuracy of our models and simulation software. Through systematic simulations, we explore the dependence of absorber bandgap on the indoor LED color temperature. The study progresses into a multi-step optimization process, targeting crucial aspects of solar cell design. Investigating interface parameters, we analyze the interplay between the conduction band offset and surface recombination velocity. Subsequently, the influence of absorber layer properties on efficiency is examined, uncovering substantial improvements by optimizing thickness and bulk defect density. Further, we scrutinize the impact of electron transport layer thickness and doping, presenting avenues for performance enhancement. Quantitative results underscore the potency of our approach. Under warm and cool LED illumination, the proposed optimizations elevate the power conversion efficiency from 10.05 to 25.58% and 9.08 to 25%, respectively, validating the effectiveness of our strategies. These findings not only underscore the viability of earth-abundant CBTSSe-based solar cells for indoor applications but also pave the way for tailored, high-efficiency low-cost energy harvesting in various indoor environments.

Keywords CBTSSe · Indoor LED · SCAPS-1D · CBO · Power conversion efficiency

1 Introduction

The rising global energy necessity and growing concerns about environmental impact impose the exploration of renewable and clean energy sources. Solar energy, among several renewable options, holds substantial prospective, where photovoltaic (PV) technology has emerged as an efficient way of directly converting solar energy into electricity (Green et al. 2023; Petrović-Ranđelović et al. 2020). Silicon (Si) solar cells currently

Extended author information available on the last page of the article

lead the PV market, representing about 93% of the market segment (Okil et al. 2022). Apart from this, thin film solar cells (TFSCs) have gained significant traction because of their notable advantages involving high power conversion efficiencies (PCEs), easy fabrication processes on flexible substrates, and low processing cost (Huang 2020; Gamal et al. 2021; Farooq et al. 2021; Ait Abdelkadir et al. 2023). These advantages have led to the widespread application of thin film PVs, particularly in building-integrated photovoltaics and other related fields.

Among TFSCs, chalcogenide compounds have garnered noteworthy scientific consideration as semiconducting materials for their tunable bandgap and potential applications in PV devices. While thin-film materials like CIGS and CdTe have proven potential for renewable energy generation, their large-scale production is hampered by the supply constraints of In, Ga, and Te (Green et al. 2021). The alloys of kesterite, specifically Cu_2ZnSnS_4 (CZTS) and $Cu_2ZnSn(S, Se)_4$ (CZTSSe), offer probable alternatives as they are composed of earth-abundant and non-toxic elements (Kumar 2021; Gohri et al. 2023; Shafi et al. 2022). Nevertheless, the performance of solar cell devices using these materials is constrained by cationic disorder and defect properties, besides their efficiency, which lags behind that of CIGSSe cells (Green et al. 2021; Sun et al. 2019). Recently, $Cu_2BaSnS_{4-x}Se_x$ (CBTSSe) has emerged as a prospective alternative due to the larger ionic radius of Ba^{2+} ($r_i = 1.56$ Å) compared to Zn^{2+} ($r_i = 0.74$ Å), offering a higher coordination number. The abundant availability of Ba, Cu, and Sn further adds to its interest as a light absorber for PV cells, surpassing the scarcity of In (Sun et al. 2019; Chakraborty et al. 2019; Ge et al. 2017a). Considerable improvements have been achieved in the synthesis of CBTSSe light absorbers and related PV devices, benefiting from theoretical insights, device structures, and functional materials. Moreover, the CBTSSe material exhibits a quasi-direct bandgap, which can be adjusted within a broad range of 1.5–2.0 eV by varying the S:Se ratio (Shin et al. 2017a). This tunability offers promising options for applications in both single-junction and multi-junction PV devices.

Numerous research studies, both experimental and simulation, have been devoted to investigating various fabrication technologies and device configurations for the CBTSSe-based solar cells. In (Shin et al. 2017b), the authors implemented a two-step process involving precursor sputter deposition and subsequent sulfurization/selenization to produce high-quality, pinhole-free CBTSSe layers incorporating selenium for high-efficiency PV devices. The incorporation of selenium enables the achievement of absorber layers within the CBTSSe with a bandgap of 1.55 eV, ideal for single-junction PV applications. Furthermore, through bandgap tunability, a CBTSSe-based PV cell with a remarkable PCE of 5.2% was reported (Shin et al. 2017b). One promising approach to boost the performance of CBTSSe-based cells is to incorporate low electron affinity (EA) electron transport materials such as $Zn_{1-x}Cd_xS$, $Zn_{1-x}Sn_xO$, and $ZnO_{1-x}S_x$ (Cui et al. 2018). An experimental study demonstrated improved open-circuit voltage (V_{OC}) and PCE by incorporating sputtered CdS:O buffer layers, suggesting that further optimization of buffer layers could lead to higher performance in CBTSSe solar cells (Ge et al. 2017b). More recently, $Zn_{1-x}Cd_xS$ (ZCS) was employed as a buffer layer with low electron affinity to enhance the band alignment between the CBTSSe absorber and the heterojunction (Cui et al. 2018). To further enhance the band alignment within the cell, a lower electron affinity (Zn, Mg)O (ZMO) and Al-doped ZnO (AZO) window layers have been incorporated. These modifications were aimed at achieving improved conduction band minimum (CBM) alignment across the entire device structure, resulting in a PCE of above 6% for the device structure AZO/ZMO/ZCS/CBTSSe/MoS_2/Mo (Teymur et al. 2022).

On the other hand, various simulation investigations have been published in the literature. In (Ghobadi et al. 2020), CBTSSe solar cells were simulated using SCAPS-1D, and the results were justified against experimental data. Various back surface field layer materials were recommended to enhance the performance. Optimization of the $MoSe_2$ layer, formed at the interface between the CBTSSe film and the Mo back electrode, was performed to determine the optimal parameters for the BSF layer. According to the various design techniques, an optimized PCE of 7.31% has been achieved, providing insights for optimizing BSF layers in CBTSSe solar cells (Ghobadi et al. 2020). In (Henni et al. 2023), the authors examined the impact of establishing an ultrathin Al_2O_3 insulating layer with a wide bandgap into a CBTS/CdS heterojunction cell, where CBTS has an energy gap of 1.9 eV. Through experimentally calibrated numerical simulations, they investigated the electron tunnelling effect within the $Mo/MoS_2/CBTS/Al_2O_3/CdS/ZnO/AZO/Al$ structure. The findings indicated that the inclusion of an Al_2O_3 layer improves the collection efficiency, leading to enhanced cell performance. Specifically, the solar cell with the $CBTS/Al_2O_3/CdS$ structure achieved a PCE of 11.89%, with V_{OC} of 1.08 V (Henni et al. 2023). Moreover, In_2S_3 thin films were numerically investigated as an ETL. An experimental CBTSSe PV cell was simulated and validated, followed by the introduction of the In_2S_3 layer as a replacement to toxic CdS. The results demonstrated that the In_2S_3 layer can effectively function as an ETL, and different variations of In_2S_3 properties were explored as potential ETLs for further optimization (Hashemi et al. 2021). When comparing the device parameters to theoretical limits, the record CBTSSe device exhibits less than 50% of the maximum voltage ratio (V_{OC}/V_{OC}^{SQ}), while optimized CZTSSe devices offer about 60% (Wang et al. 2014). Despite some improvements, CBTSSe devices still face a significant V_{OC} deficit. To address this issue and assess suitability for practical applications, it is crucial to gather information on defects, carrier lifetime, density, mobility, absorber band levels and more. Moreover, a comprehensive simulation of CBTSSe solar cell devices is crucial to accelerate their development.

As indoor lighting predominantly involves LED sources, which emit light within a specific range of wavelengths and specific color temperatures, having an absorber material with a bandgap optimized for the different conditions is crucial for enhancing energy harvesting efficiency. The unique property of CBTSSe as a tunable bandgap material allows for the adjustment of its bandgap within the specific range 1.7–1.9 eV, a range that aligns well with the spectral emission of LED illumination commonly used indoors. Therefore, in this paper, we investigate the suitability of CBTSSe-based PV cells having wide bandgaps for indoor applications. Our investigation begins by designing the solar cell device structure, adhering to the ITO/i-ZnO/CdS/absorber/Mo/glass layer sequence, based on an experimental work (Shin et al. 2017b). By replicating the terminal characteristics of the PV cell by simulation under AM1.5G illumination, we provide a validation of the models employed. Next, we present the design of the CBTSSe solar cell under warm and cool LED illumination conditions. Multiple factors impacting CBTSSe solar cell performance across varying LED spectra are investigated. The core objective of this study is to achieve the optimization of cell performance through an in-depth analysis of the intricate interplay between key parameters. Following an initial investigation into the role of the absorber bandgap, we embark on an intricate optimization procedure aimed at designing the solar cell to achieve the utmost achievable PCE. The optimization process unfolds through three main steps, each addressing a different aspect of the cell design. These stages encompass the meticulous management of interface parameters (CBO and S), absorber layer parameters (thickness and bulk defects), and ETL parameters (thickness and doping). Finally, we provide a comprehensive overview of

the optimization process. By encapsulating an array of simulations and investigations, this study is poised to not only advance the understanding of CBTSSe solar cell performance but also offer critical insights into the intricate relationship between material parameters and device efficiency. This understanding is anticipated to significantly contribute to the advancement of wide-bandgap solar cell technologies optimized for indoor applications.

2 Simulation method and device configuration

2.1 SCAPS simulator

In this study, we utilize the SCAPS-1D software, evolved by the University of Ghent, Belgium, to simulate and calculate the key PV parameters of the CBTSSe-based thin-film solar cell. SCAPS-1D is a one-dimensional PV cell device simulator program primarily designed for TFSCs. The simulator accurately calculates the performance metrics of the PV devices using numerical solutions of fundamental semiconductor equations. These equations are solved self consistently until convergence is met. Poisson's equation (Eq. (1)) is used to describe the electrostatic potential Ψ within the semiconductor material. The continuity equations (Eq. (2)) describe the continuity of charge carriers (electrons and holes) in a certain semiconductor region. They are crucial for modeling carrier transport and recombination. The bulk Shockley–Read–Hall (SRH) recombination equation (Eq. (3)) calculates the recombination rate due to bulk defects, while the interface SRH recombination equation (Eq. (4)) accounts for recombination at the interfaces between the distinct layers. Finally, the transport equations (Eq. (5)) govern the transport of holes and electrons within the material under consideration. They are basically based on the drift–diffusion approach. Regarding the mobility modeling, the electron and hole mobilities are taken to be constants (constant mobility model).

$$\frac{d^2\Psi}{dx^2} = \frac{q}{\varepsilon}(n - p + N_A^- - N_D^+ + n_t - p_t) \tag{1}$$

The ionized acceptor and donor doping concentrations are denoted by N_A^- and N_D^+. The free electron and hole concentrations are termed n, and p, while the corresponding trap densities are n_t and p_t.

$$\frac{1}{q}\frac{dJ_n}{dx} = U_n - G(x)$$
$$\frac{1}{q}\frac{dJ_p}{dx} = G(x) - U_p \tag{2}$$

The terms U_n and U_p represent carrier recombination rates, while G is the generation rate due to a light source (either AM1.5G or due to LED illumination, etc.).

$$R_{SRH,bulk} = \frac{(np - n_i^2)}{\tau_p(n + n_1) + \tau_n(p + p_1)} \tag{3}$$

τ_n and τ_p are bulk minority carrier lifetimes for electrons and holes.

$$R_{SRH,int} = \frac{(n_{if}p_{if} - n_i^2)}{\frac{p_{if}+p_1}{S_n} + \frac{n_{if}+n_1}{S_p}} \tag{4}$$

S_n and S_p are the interface recombination velocities for electrons and holes.

$$J_n = qn\mu_n E + qD_n\frac{dn}{dx}$$
$$J_p = qp\mu_p E - qD_p\frac{dp}{dx} \tag{5}$$

D_n and D_p represent the electron and hole diffusion coefficient, while μ_n and μ_p denote the electron and hole mobility. The electric field is denoted by E.

Upon performing the solution, many terminal characteristics and physical parameters can be extracted such as the current density versus voltage (J–V) and external quantum efficiency (EQE), recombination rates, electric field, energy band profiles and other useful characteristics. Other crucial parameters such as PCE, V_{OC}, J_{SC} (short-circuit current), and FF (fill factor) can also be easily extracted.

2.2 Solar cell arrangement and materials

The solar cell device construction is designed based on a fabricated PV cell incorporating the following layer sequence: ITO/i-ZnO/CdS/$Cu_2BaSnS_{4-x}Se_x$/Mo/glass, where x = 3. Figure 1a demonstrates the PV cell structure, while Fig. 1b illustrates the conduction band minimum (CBM) and valence band maximum (VBM) for all cell layers. The CdS thickness is 50 nm, while the thicknesses of i-ZnO and ITO are 50 nm and 150 nm, respectively. The absorber thickness is about 1 μm, while its measured bandgap is about 1.54 eV (Shin et al. 2017b). Regarding the work functions of the electrodes, they are adjusted at 4.4 eV for the front ITO contact and 5 eV for the back Mo contact. Most of the defect parameters are obtained from Ref (Shin et al. 2017b), while some other parameters are optimized to fit the experimental data. All other material properties and parameters as well as bulk and interface defects used in SCAPS simulations are extracted from relevant literature as listed in Tables 1 and 2. Further, the energy band profile after contact at short-circuit condition is displayed in Fig. 1c (given AM1.5G illumination).

2.3 SCAPS calibration

The following simulations are conducted at an operating temperature of 300 K, with AM1.5G light illumination (1000 W/m^2). The reference experimental cell detailed in Shin et al. (2017b) was replicated in the SCAPS software. The alignment of the simulated results in the SCAPS environment was achieved by utilizing the physical material parameters outlined in Tables 1 and 2. Upon using these parameters and running the simulator, decent agreement between the experimental and SCAPS outcomes is observed, as presented in Fig. 2a, which shows the J–V characteristic curves of both simulated and experimental PV cells. Further, in order to quantitatively validate the simulated results from the SCAPS simulator against the experimental work, we compared the functional PV metrics of the simulated solar cell versus the results from the experimental cell as reported in Shin et al. (2017b). The congruence between the SCAPS results and the experimental outcomes is evident from the data provided
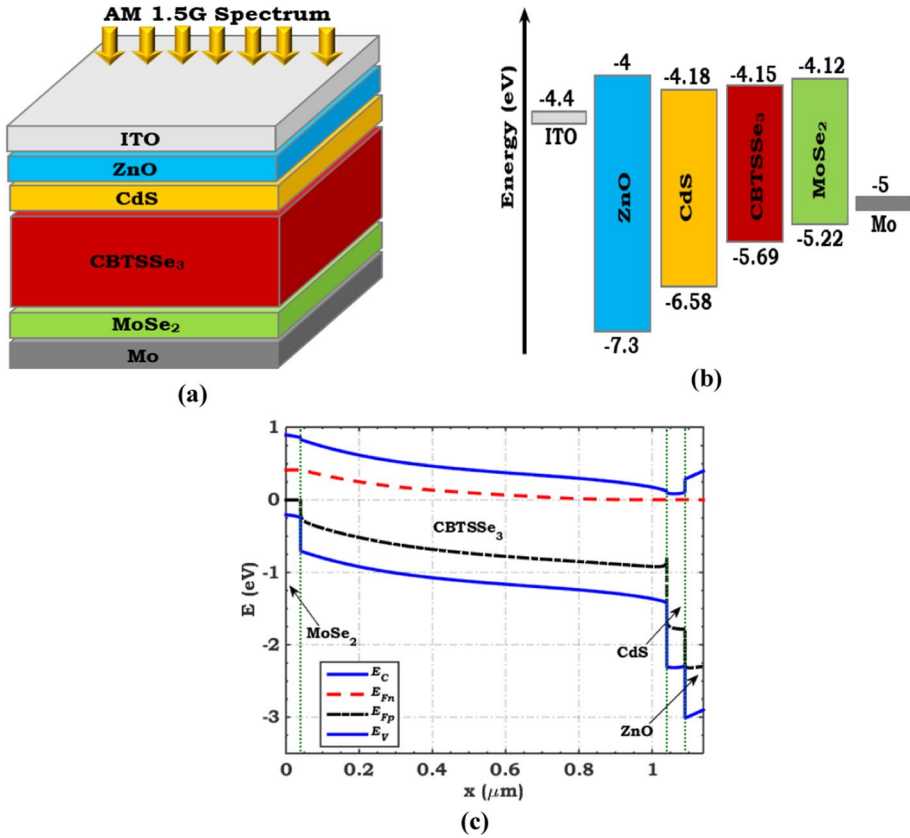
Fig. 1 Typical CBTSSe cell configuration: **a** main cell layers, **b** energy band profile before contact illustrating the accompanying energy levels of each thin film, and **c** energy band diagram after contact at short circuit current condition under AM1.5G illumination

in Fig. 2a, where PV parameters, including: PCE of 5.27%, V_{OC} of 0.618 V, J_{SC} of 17.32 mA/cm^2, and FF of 49.17%, were adopted, as highlighted in the figure. The values of the main simulated PV metrics closely align with those obtained experimentally, with a percentage error of just 1.35% for PCE. In addition, EQE characteristic curves of experimental and simulated CBTSSe cells (Shin et al. 2017b) are presented in Fig. 2b, utilizing the given parameters. It is prominent to notice that the simulated EQE-derived photocurrent is 17.32 mA/cm^2, which closely matches the measured J_{SC} under AM1.5G illumination condition (17.40 mA/cm^2). The findings revealed in Fig. 2 underscore the accuracy of the applied models and the merit of the software utilized in this study. It should be pointed out here that the experimental EQE-derived photocurrent is 17.59 mA/cm^2, which is higher than the experimental J_{SC} derived from the J–V curve. This can be attributed to the different conditions of measurements regarding the J–V and EQE curves.

Table 1 Major physical parameters of the materials used in this work

Parameters	ZnO	CdS	CBTSSe$_3$	MoSe$_2$	Cd$_{0.4}$Zn$_{0.6}$S
Layer thickness, t (nm)	50	50	1000	40	50
Energy gap, E_g (eV)	3.3	2.4	1.54	1.1	2.88
Electron affinity, χ (eV)	4	4.18	4.15	4.12	3.85
Relative permittivity, ε_r	9	10	5.5	8.76	9
Effective DOS in valence band, N_v (cm^{-3})	1.9×10^{19}	1.9×10^{19}	3.42×10^{19}	2.65×10^{19}	2.2×10^{18}
Effective DOS in conduction band, N_c (cm^{-3})	2.2×10^{18}	2.5×10^{18}	1.76×10^{18}	2.8×10^{19}	1.8×10^{19}
Hole mobility, μ_p (cm^2 V^{-1}s^{-1})	25	25	1.5	50	25
Electron mobility, μ_n (cm^{2}V^{-1}s^{-1})	100	100	1	100	100
Acceptor density, N_A (cm^{-3})	–	–	5×10^{14}	1×10^{16}	–
Donor density, N_D (cm^{-3})	1×10^{10}	1.25×10^{17}	–	–	1×10^{17}
Reference	Salah et al. (2019)	Salem et al. (2022a)	Shin et al. (2017b); Teymur et al. (2021)	Moustafa et al. (2021)	Salem et al. (2022b)

Table 2 Defects parameters of the cell layers and at the interfaces

	ZnO	CdS	CBTSSe$_3$	MoSe$_2$	CdS/CBTSSe$_3$
Defect type	Neutral	Neutral	Donor	Neutral	Donor
Carrier capture cross section	1×10^{-15} cm^2	1×10^{-15} cm^2	1×10^{-15} cm^2	1×10^{-15} cm^2	1×10^{-15} cm^2
Energetic distribution	Gaussian	Gaussian	Gaussian	Gaussian	Gaussian
Energy level with respect to the highest E_v	1.5 eV	1 eV	0.75 eV	0.6 eV	0.75 eV
Concentration	1×10^{15} cm^{-3}	1×10^{15} cm^{-3}	2.3×10^{15} cm^{-3}	1×10^{15} cm^{-3}	1×10^{15} cm^{-2}
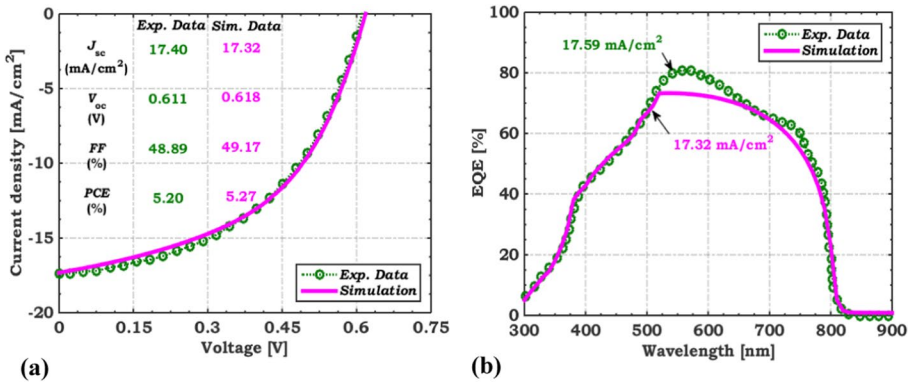
Fig. 2 Calibration of simulation versus experimental data (Shin et al. 2017b) **a** *J–V* curves under AM1.5G illumination, and **b** EQE curves

3 Results and discussion

In this section, we delve into the outcomes of our simulations and investigations, exploring various factors that influence the performance of CBTSSe solar cells under different LED color temperatures. The design of the CBTSSe cell is based on identifying the influence of the main factors of the cell on its performance so as to reach the best PCE. The optimization procedure is divided into three main steps concerning the interface between the photoactive layer and the ETL, the photoactive layer and the ETL. The following subsections highlight the key aspects examined in this study, shedding light on their effects on the PCE and characteristics of the PV cells. In the first subsection, the role of absorber bandgap is explored to validate the appropriate bandgap value that best suits the LED spectra. In the second subsection, the interface parameters are investigated by simultaneously studying the influence of the CBO and S between the absorber and ETL heterointerface. The subsequent subsection is devoted to the impact of absorber layer parameters on the performance through studying the thickness and bulk defect influence. Further, the influence of thickness and doping of the ETL is presented in the fourth subsection. Finally, the optimization phases are summarized in the last subsection, giving a comparison between each step, and explaining the physics beyond the behavior of the PV device.

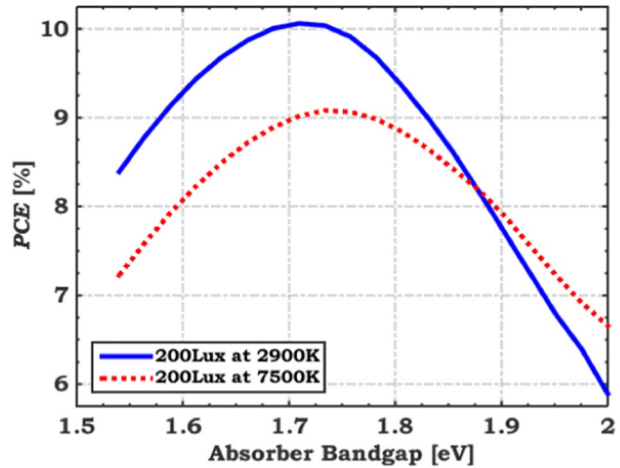**Fig. 3** Dependence of PCE on absorber bandgap under different LED spectra

Table 3 Main absorber and performance parameters of CBTSSe cell under different LED temperatures at optimum bandgap values

Spectrum	E_g (eV)	χ_{abs} (eV)	J_{SC} ($\mu A/cm^2$)	V_{OC} (V)	FF (%)	PCE (%)
200 lx at 2900K	1.70	3.99	17.94	0.605	53.59	10.05
200 lx at 7500K	1.73	3.96	19.07	0.636	52.47	9.08

3.1 Role of absorber bandgap

Here, we thoroughly examine the role of CBTSSe absorber bandgap under different LED color temperatures. Specifically, we investigate the warm and cool LED effects by analyzing two cases: LED color temperatures of 2900 K and 7500 K. For the two cases, the illumination is taken to be fixed at 200 lx. Figure 3 illustrates the relationship between PCE and absorber bandgap across different LED temperatures. The findings indicate that, for our particular design, an optimal bandgap of 1.70 eV aligns with the 2900 K LED spectrum, while a bandgap of 1.73 eV is most proper for the 7500 K LED spectrum. The subtle disparity between these two bandgap values suggests that any value within this range of E_g (1.70–1.73 eV) could be effectively employed for both temperature scenarios. The main absorber and performance parameters of CBTSSe cell at optimum bandgap values are listed in Table 3. It should be pointed out here that the color temperature of LED sources indicates the energy of their emitted photons, with higher temperatures yielding higher-energy photons. Solar cell efficiency relies on aligning the cell's bandgap energy with incident photon energy to avoid energy waste or inadequate electron–hole pair creation. To minimize parasitic effects, such as thermalization occurring for $E_{photon} \gg E_g$, it is crucial to match absorber bandgap with LED spectra, making high band gaps suitable for high-temperature LEDs and low band gaps for low-temperature LEDs.

Additionally, we proceed to generate the EQE curves for the initial CBTSSe cell, utilizing the optimized bandgap values, as depicted in Fig. 4. This graph presents the EQE curves for the CBTSSe cell with the optimized bandgaps, under LED Spectra of 200 lx at 2900K and

Fig. 4 EQE curves of initial CBTSSe cell with optimized bandgaps under 200 lx LED Spectra at 2900K, and 7500K showing corresponding LED spectra
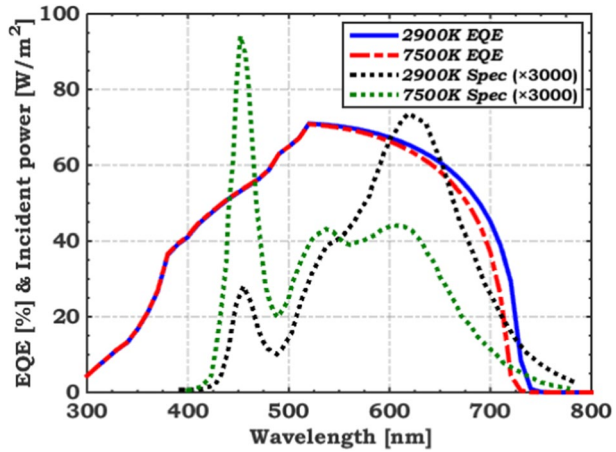
7500K, accompanied by the respective LED spectra. The figure notably illustrates the favorable alignment of the optimized-bandgap CBTSSe material with the spectral range of LED illumination. This alignment underscores the efficacy of the chosen bandgaps in maximizing energy harvesting efficiency under both warm and cool LED conditions.

3.2 Effect of interface parameters (CBO and S)

The interplay between the conduction band offset (CBO) and surface recombination velocity (S) at the heterointerface of a solar cell is crucial for determining the device's performance. The heterointerface between the absorber and ETL plays a substantial role in charge carrier extraction, recombination, and overall device efficiency (Minemoto and Murata 2015; Okil et al. 2023), and it is described as,

$$CBO = \Delta E_c = \chi_{absorber} - \chi_{ETL} \tag{6}$$

where $\chi_{absorber}$ and χ_{ETL} are the affinities of the absorber and the ETL, respectively.

Figure 5 shows two different band profiles, representing different values of CBO. Figure 5a shows the cliff band case, which does not deter the extraction of photoexcited electrons from the absorber to the ETL. Still, it alters the activation energy (E_a) that is related to the charge carrier recombination. In this scenario, the activation energy is less than the absorber bandgap (E_g) as can depicted in Fig. 5a. As a result, interfacial recombination losses become the dominant recombination process within the cell (Minemoto and Murata 2015; Tanaka et al. 2009). Conversely, Fig. 5b demonstrates the formation of a spike-like band offset at the ETL/Absorber interface. This spike creates an obstacle to the extraction of the photoexcited electrons from the absorber towards the front electrode (Scheer and Schock 2011). Nevertheless, when the spike is low enough, it no longer has any effect, and the electrons can flow smoothly towards the contact. An optimal CBO ensures balanced carrier injection and reduced recombination.

S quantifies the rate at which charge carriers recombine at the interface, and it is described as,
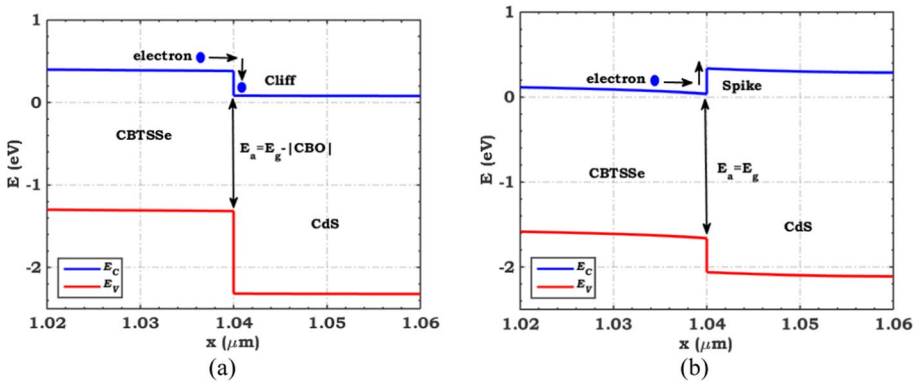
$$S = \sigma N_t v_{th} \tag{7}$$

Fig. 5 Energy band diagrams of two cases of CBOs **a** a cliff-like band offset, and **b** a spike-like band offset

where σ is the carrier capture cross section, N_t is the interface defect density, and v_{th} is the thermal velocity. Higher S values indicate more rapid recombination, potentially leading to lower charge carrier extraction efficiency, while a lower S value is desirable as it extends the carrier lifetime and reduces recombination losses. Also, a lower S value allows carriers to reach the contacts before recombination occurs, leading to improved charge extraction efficiency and higher V_{OC}. An optimal combination of CBO and S is necessary to strike a balance between carrier injection and extraction. A positive CBO should be matched with a lower S value to minimize recombination at the heterointerface. The CBO-S interplay influences the dynamics of charge carriers as they traverse the heterointerface. Proper alignment enhances carrier transport through the interface, reducing the probability of recombination.

This subsection delves into the influence of CBO and S on the CBTSSe cell performance. We investigate these factors for two different LED spectra (LED 200 lx at 2900K and 7500K) and corresponding bandgap values. By mapping out contour plots of key PV parameters, including J_{SC}, V_{OC}, FF, and PCE, we uncover the optimal ranges of CBO and S that yield the highest efficiency. In this theoretical investigation, CBO is changed from -0.3 to 0.3 eV, while S is varied from 10^4 to 10^7 cm/s. Figure 6 shows contour plot of PV performance factors for CBTSSe cell under LED 200 lx at 2900K spectrum at different CBO and S values. Similarly, contour plots under LED 200 lx at 7500K spectrum are depicted in Fig. 7.

The investigation into the CBO and S reveals an optimum CBO range across various LED spectra, spanning from 0.1 to 0.3 eV. Within this specified CBO range and at a constant S of 10^5 cm/s, the PCE of the CBTSSe cell demonstrates a slight enhancement. Specifically, for the 2900K LED temperature, the PCE experiences an increment from 11.87 to 11.95% within this CBO range. In parallel, for the 7500K LED temperature, a similar trend is observed, albeit with slightly different numerical values. Here, the PCE transitions from 11.45 to 11.54% as the CBO varies within the prescribed optimal range. These results underscore the sensitivity of the CBTSSe solar cell performance to the CBO, particularly within the specified CBO range, which showcases the direct correlation between CBO and PCE under different LED temperature conditions. Furthermore, at $S = 10^5$ cm/s, we draw the interface recombination current density for three distinct CBO values, as indicated in Fig. 8. The results reveal that the recombination current density decreases significantly with optimum CBO values under different LED
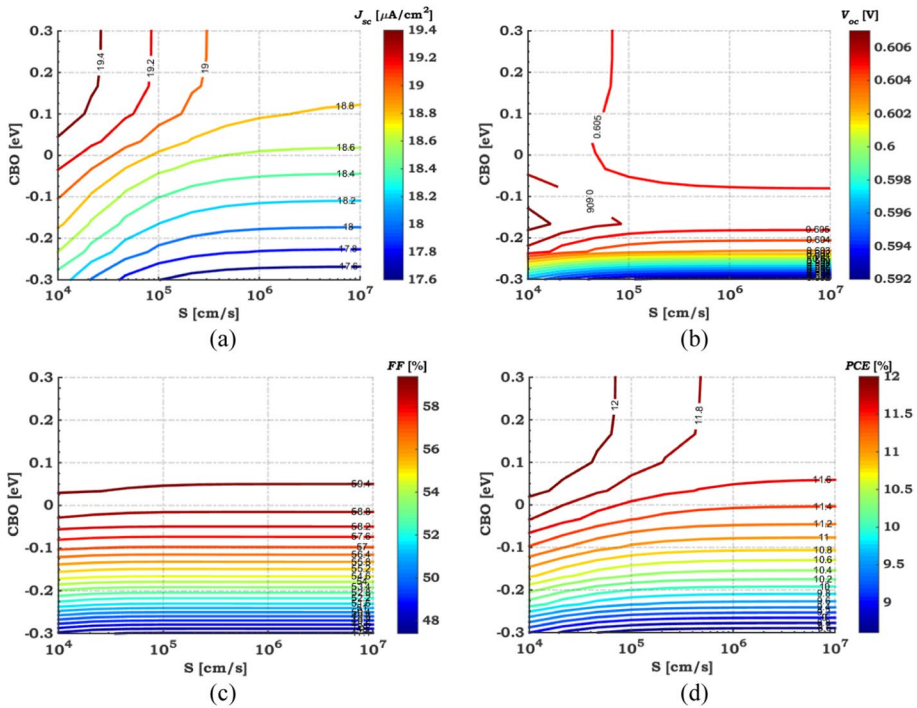
Fig. 6 Contour plots of PV metrics for CBTSSe cell: **a** J_{SC}, **b** V_{OC}, **c** FF and **d** PCE under LED 200 lx at 2900K spectrum at different CBO and S values

temperature conditions. This finding confirms the importance of CBO engineering in reducing interfacial recombination.

As the optimum CBO range under different spectrums is from 0.1 to 0.3 eV, $Cd_{0.4}Zn_{0.6}S$ can be utilized as an ETL instead of CdS because of its optimum CBO values of 0.14 eV and 0.11 eV under LED 200 lx at 2900K and 7500K, respectively. The simulation parameters of the ternary alloy $Cd_{0.4}Zn_{0.6}S$ are given in Table 1 (Salem et al. 2022b). In this case, performance parameters of CBTSSe cell are a PCE of 12.06%, V_{OC} of 0.605 V, J_{SC} of 19.34 µA/cm^2, and FF of 59.65% under LED 200 lx at 2900K, while they are a PCE of 12.02%, V_{OC} of 0.639 V, J_{SC} of 21.94 µA/cm^2, and FF of 60.15% under LED 200 lx at 7500K.

3.3 Effect of absorber parameters (thickness and bulk defects)

The interplay between the thickness and defect concentration of the absorber layer in a PV cell is a crucial aspect that significantly affects the device's overall performance. Notably, the thickness of the absorber film directly affects the amount of incident light that is absorbed. A thicker absorber can absorb more light leading to higher electron–hole generation and improved J_{SC}. However, if the absorber becomes too thick, it might lead to increased recombination losses, as charge carriers may not efficiently reach the contacts before recombining. In line with this, defects within the absorber film act as recombination centers, facilitating charge carrier recombination. Higher defect densities can lead to
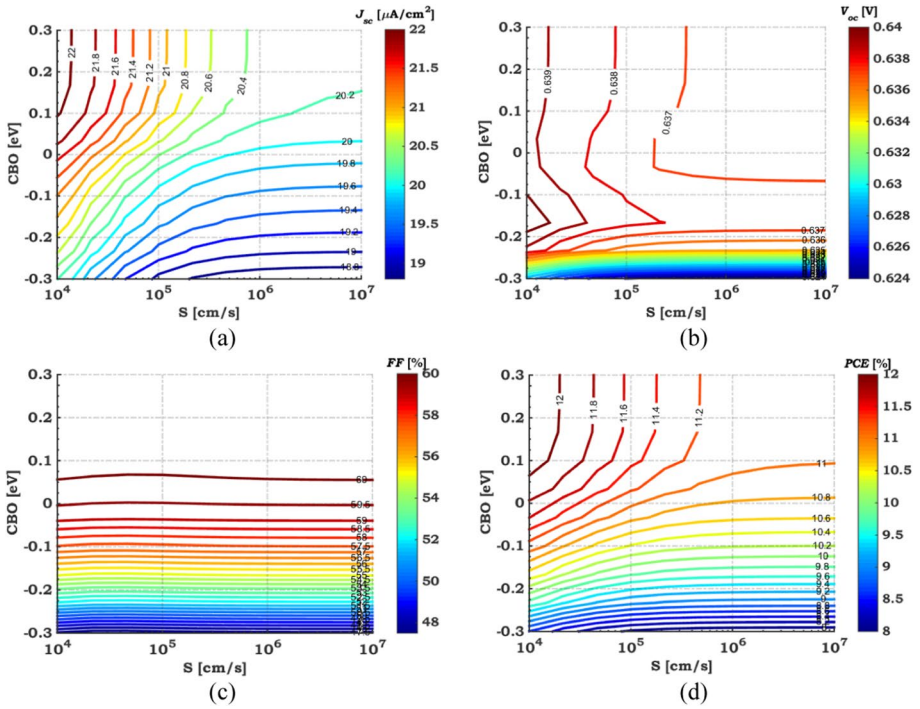
Fig. 7 Contour plots of PV metrics for CBTSSe cell: **a** J_{SC}, **b** V_{OC}, **c** FF and **d** PCE under LED 200 lx at 7500K spectrum at different CBO and S values
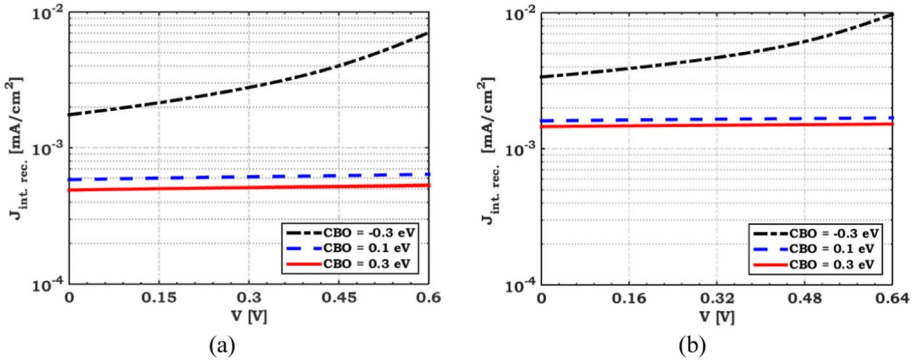

Fig. 8 Interface recombination current density for CBTSSe cell under LED 200 lx at **a** 2900K, and **b** 7500K

increased non-radiative recombination, reducing the carrier lifetime and thereby decreasing V_{OC} and FF. Lower defect densities are preferred to minimize recombination losses and enhance the overall cell performance. The interplay between thickness and defect density is particularly pronounced in their effects on V_{OC} and FF. Higher defect densities in a thicker absorber layer can cause more pronounced recombination, leading to a decrease in

V_{OC} due to a higher recombination current. Moreover, the decreased FF is often attributed to enhanced recombination-related voltage losses as carriers traverse the device. Balancing the thickness and defect density involves optimization to achieve the best compromise between enhanced light absorption and reduced recombination losses. It is essential to find the sweet spot where the trade-offs between increased light absorption and the negative impact of defects on carrier dynamics are minimized.

Here, we explore the influence of absorber thickness and bulk defect density on the CBTSSe cell's efficiency. Extending our analysis to both LED 200 lx spectra at 2900K and 7500K, we construct contour plots for J_{SC}, V_{OC}, FF, and PCE, revealing the intricate interplay between these parameters. By selecting a representative thickness and defect density, we provide a detailed examination of the cell's performance under these conditions. In this theoretical investigation, defect density of the absorber layer is changed from 10^{12} to 10^{15} cm^{-3}, while its thickness is varied from 0.5 to 5 μm. Figures 9 and 10 show contour plots of PV performance factors for the CBTSSe cell under LED 200 lx at 2900K and 7500K spectrum at different defect density and thickness values, respectively. The observed trends are consistent across various temperatures, as depicted in both figures. The PCE demonstrates an upward rise with increasing thickness, holding a constant defect density level. However, the PCE tends to reach a nearly saturation point as the thickness continues to increase beyond a certain threshold. The optimum choice is selected to be a thickness of 2 μm and defect density of 1×10^{14} cm^{-3}. In this case, PV parameters of CBTSSe cell are a PCE of 20.75%, V_{OC} of 0.796 V, J_{SC} of 21.59 μA/cm^2, and FF of 69.95% under LED 200 lx
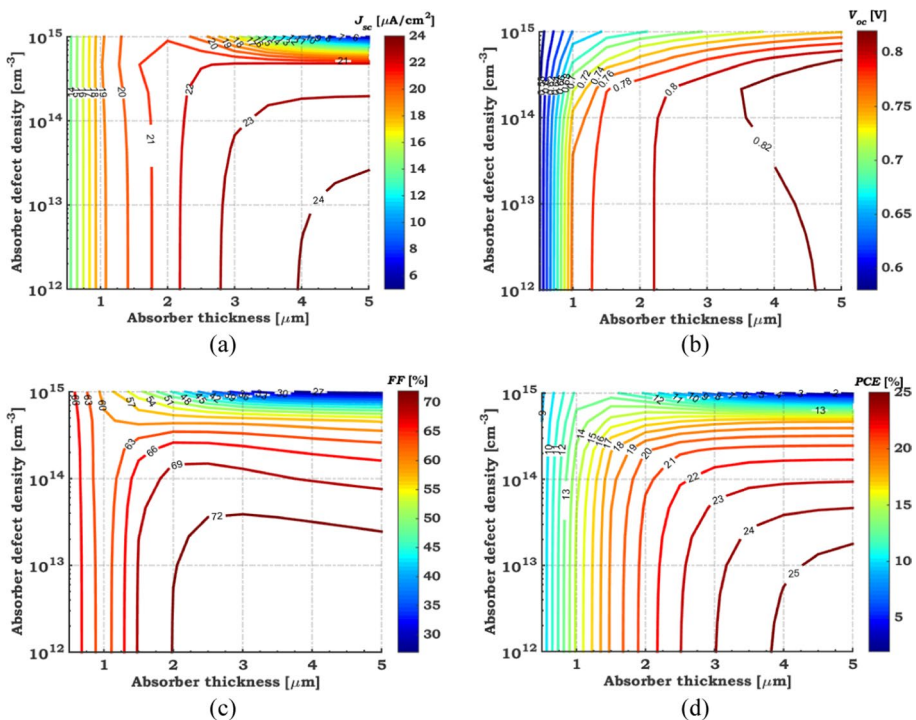

Fig. 9 Contour plots of PV metrics for CBTSSe cell: **a** J_{SC}, **b** V_{OC}, **c** FF and **d** PCE under LED 200 lx at 2900K spectrum at different thickness and bulk defect concentration of the absorber layer
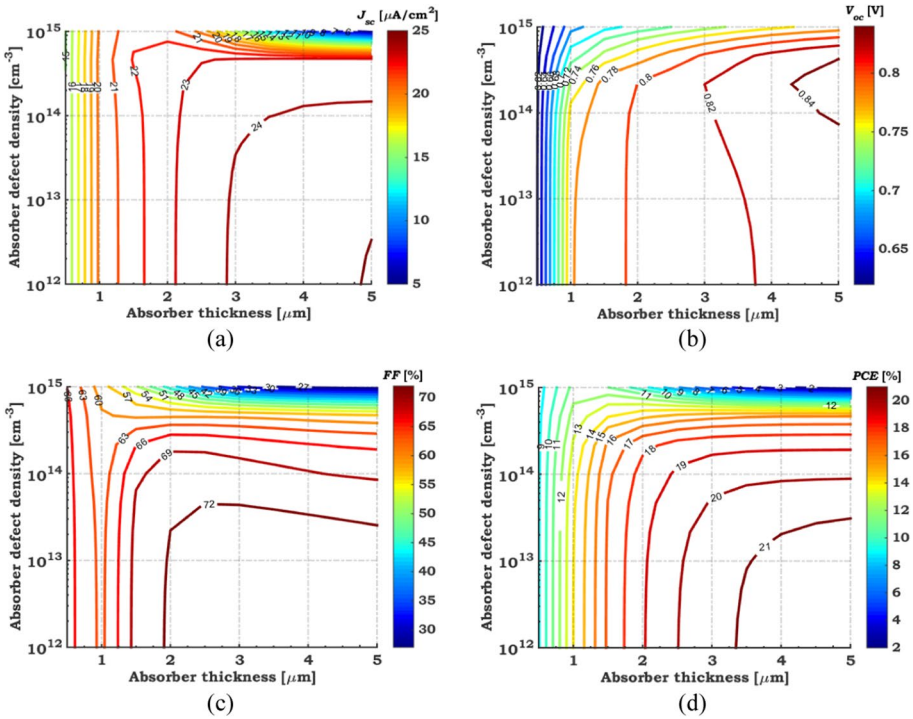
Fig. 10 Contour plots of PV metrics for CBTSSe cell: **a** J_{SC}, **b** V_{OC}, **c** FF and **d** PCE under LED 200 lx at 7500K spectrum at different thickness and bulk defect concentration of the absorber layer

at 2900K, whereas they are a PCE of 18.36%, V_{OC} of 0.802 V, J_{SC} of 22.75 µA/cm^2, and FF of 70.51% under LED 200 lx at 7500K.

3.4 Effect of ETL parameters (thickness and doping)

Notably, the thickness of the ETL directly affects the ease of charge transport within the layer. A thicker ETL might increase the distance that charge carriers need to travel, leading to a longer transit time and potentially higher recombination losses. Conversely, a thinner ETL can facilitate faster carrier extraction and transport to the external circuit, resulting in improved device performance. In addition, the doping density of the ETL determines the concentration of charge carriers (usually electrons) available for transport. Higher doping densities increase the density of free electrons, enhancing the electrical conductivity of the ETL. This can lead to improved carrier extraction efficiency and reduced resistive losses. Striking a balance between thickness and doping density is crucial to prevent excessive recombination. Very high doping densities can lead to increased trap-assisted recombination, especially if the ETL is too thick, as carriers might have a higher probability of interacting with defects and traps.

By creating contour plots of PCE dependence on thickness and doping of the ETL under LED 200 lx at both 2900K and 7500K, we uncover the optimized regions for these parameters. We present performance parameters for the CBTSSe cell at specific thickness and doping levels, providing insights into the role of ETL characteristics in determining the
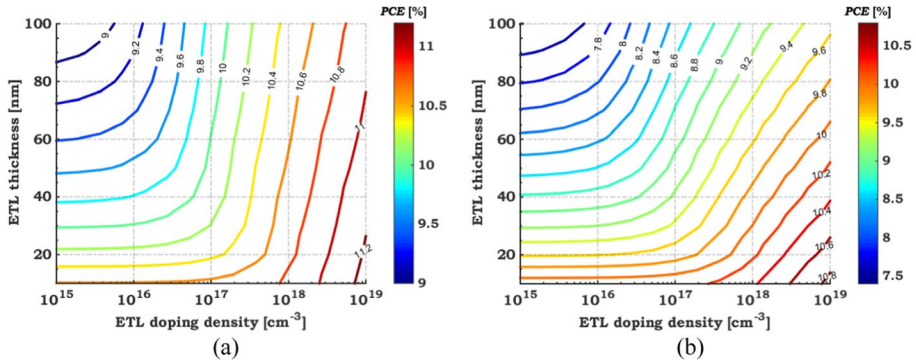
Fig. 11 Contour plot of PCE for CBTSSe cell at different thickness and doping of the ETL layer under LED 200 lx at **a** 2900K and **b** 7500K

cell's efficiency. Figure 10 shows contour plots of PCE for CBTSSe cell under LED 200 lx at 2900K (Fig. 11a) and 7500K (Fig. 11b) spectrum at different thickness and doping values. As anticipated, the PCE exhibits higher values within regions characterized by thinner and more heavily doped ETL. At a thickness of 20 nm and a doping level of 1×10^{19} cm^{-3}, performance parameters of CBTSSe cell are: PCE of 11.23%, V_{OC} of 0.605 V, J_{SC} of 18.54 µA/cm^2, and FF of 57.95% under LED 200 lx at 2900K, whereas they are a PCE of 10.70%, V_{OC} of 0.639 V, J_{SC} of 20.41 µA/cm^2, and FF of 57.54% under LED 200 lx at 7500K.

3.5 Final optimization

In the final subsection, we bring together the cumulative insights from the previous analyses and present the ultimate optimization stages for the CBTSSe solar cell. We compile performance parameters under optimal conditions in a comprehensive table, showcasing the improvements achieved. Calculated efficiency enhancements are presented as relative percentages under LED 200 lx spectra at 2900K and 7500K. We compare the illuminated *J–V* characteristics of the initial and final optimized CBTSSe cells, offering a visual representation of the enhanced performance. To further understand the underlying physics of the observed trends, we analyze the electric field distribution under illuminated short-circuit conditions for both initial and optimized cells. This subsection concludes the section by summarizing the achieved optimizations and their implications for enhancing CBTSSe solar cell efficiency.

Table 4 summarizes the optoelectronic parameters of the CBTSSe cell during various optimization stages under LED 200 lx spectra at the two studied color temperatures. Further, Fig. 12a and b depicts PCE of the different optimization stages and the enhancement percentage in PCE over the initial stage. Based on the results, the most substantial factors, that influence cell performance, among the various factors are the defect concentration and thickness of the photoactive layer, which provide 106.47% and 102.20% enhancement relative percentages under LED 200 lx spectra at 2900K and 7500K, respectively.

In addition, Fig. 13a and b display the illuminated *J–V* characteristics curves of initial and final optimized CBTSSe cells under LED 200 lx spectra at 2900K and 7500K. The significant enhancement in cell performance can be accredited to the comprehensive

Table 4 Performance parameters of CBTSSe under optimization stages

| Spectrum	E_g (eV)	Layer	Parameter	J_{SC} (μA/cm^2)	V_{OC} (V)	FF (%)	PCE (%)	ξ (%)
200 lx at 2900K	1.70	Initial		17.94	0.605	53.59	10.05	–
		Interface	CBO & S	19.34	0.605	59.65	12.06	20
		Absorber	t & $N_{t,bulk}$	21.59	0.796	69.95	20.75	106.47
		ETL	t & N_D	18.54	0.605	57.95	11.23	11.74
		Final optimized		23	0.898	71.76	25.58	154.53
200 lx at 7500K	1.73	Initial		19.07	0.636	52.47	9.08	–
		Interface	CBO & S	21.94	0.639	60.15	12.02	32.38
		Absorber	t & $N_{t,bulk}$	22.75	0.802	70.51	18.36	102.20
		ETL	t & N_D	20.41	0.639	57.54	10.70	17.84
		Final optimized		25.67	0.932	73.24	25	175.33
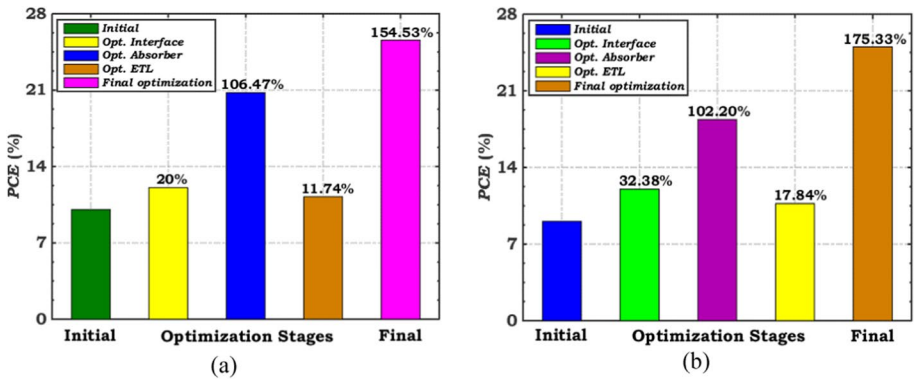
Fig. 12 Calculated efficiency improvements for CBTSSe cell showing the enhancement relative percentage under LED 200 lx at **a** 2900K, and **b** 7500K
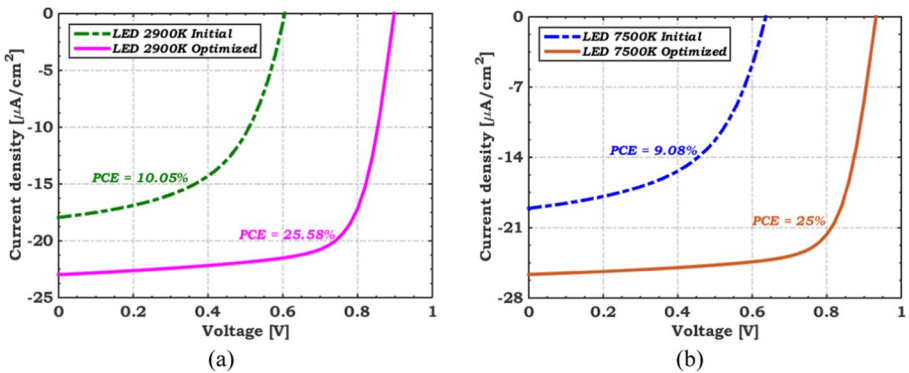

Fig. 13 A comparison between illuminated *J–V* curves of initial and final optimized CBTSSe cells under LED 200 lx at **a** 2900K, and **b** 7500K

optimization procedures that led to achieving remarkable PCEs of 25.58% and 25%, accompanied by relative percentage improvements of 154.53% and 175.33%, compared to the initial cell under LED 200 lx spectra at 2900K and 7500K, respectively. To further give a physical explanation about these improvements in cell performance, the electric field distribution is plotted under illuminated and short-circuit conditions for initial and final optimized CBTSSe cells, as depicted in Fig. 14a (for the case of 2900K) and Fig. 14b (for the case of 7500K). As illustrated in the figure, according to the optimization steps, the electric field is substantially increased, leading to accelerated separation of photoexcited carriers, reduced recombination rates, and enhanced cell performance. Moreover, Fig. 15a and b display the energy band profiles of final optimized CBTSSe cells at short circuit current condition under LED 200 lx at 2900K, and 7500K, respectively.

4 Conclusion

In conclusion, this study has systematically examined the feasibility of employing CBTSSe-based solar cells with wide bandgaps for indoor applications. The unique tunable bandgap property of CBTSSe was harnessed to tailor the absorber material's
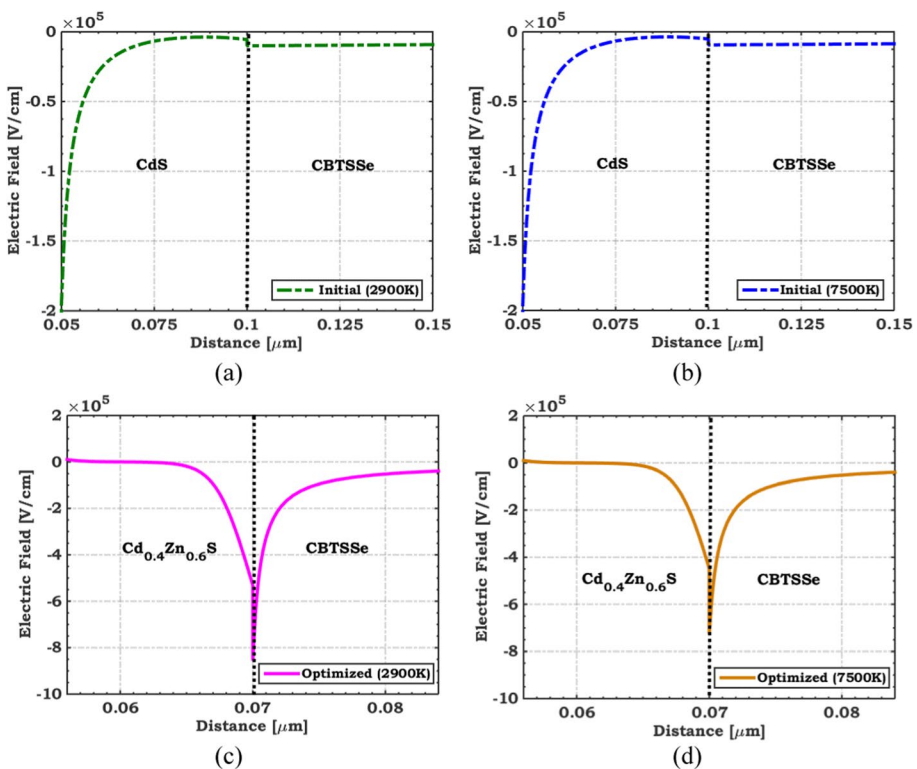

Fig. 14 Electric field distribution plotted under illuminated short-circuit condition for an initial CBTSSe cell under LED 200 lx at **a** 2900K, and **b** 7500K and the final optimized CBTSSe cell under LED 200 lx at **c** 2900K, and **d** 7500K
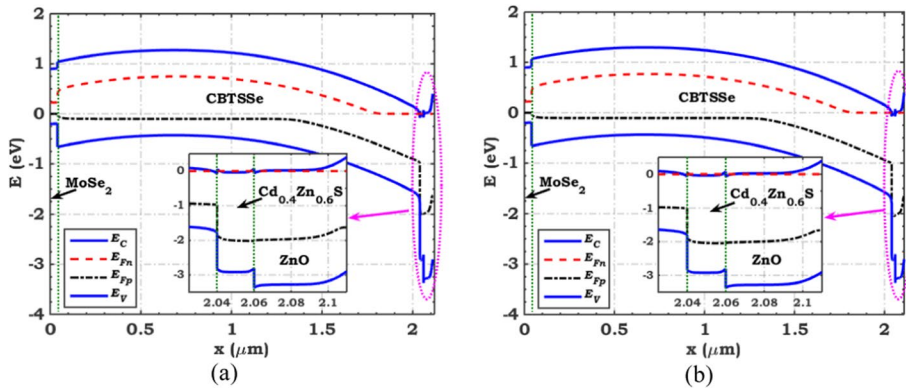
Fig. 15 Energy band profile at illumination and short circuit condition of final optimized CBTSSe cells under LED 200 lx at **a** 2900K, and **b** 7500K

characteristics within the 1.7–1.9 eV range, aligning aptly with the spectral emission of commonly used indoor LED lighting. Our investigations encompassed a meticulous design of the solar cell device structure, which was validated through simulation against experimental results, thus ensuring the fidelity of our models and the proficiency of the software employed. Throughout the study, a comprehensive exploration of factors influencing CBTSSe solar cell performance under varying LED spectra was undertaken. We meticulously delved into the role of absorber bandgap under warm and cool LED illumination conditions to determine the suitable bandgap range for various LED environment. For our particular design, an optimal bandgap of 1.70 eV with a PCE of 10.05% aligns with the 2900 K LED spectrum, while a bandgap of 1.73 eV with a PCE of 9.08% is most suitable for the 7500 K LED spectrum. Subsequent to this analysis, our focus extended to a three-step optimization procedure, each dedicated to refining a specific facet of the solar cell design. These phases entailed the intricate management of interface parameters, the meticulous adjustment of absorber layer properties, and the astute manipulation of ETL attributes.

Our findings demonstrated the criticality of interface parameters; with an optimum CBO range of 0.1 to 0.3 eV, the PCE was enhanced up to 12.06% under the warm LED spectrum and 12.02% under the cool LED spectrum. The thickness and bulk defect density of the photoactive film were also found to play pivotal roles, showcasing the potential for efficiency improvements, resulting in a PCE of 20.75% under the warm LED spectrum and 18.36% under the cool LED spectrum. Moreover, adjustments to the ETL layer parameters exhibited tangible gains, with the potential for PCE improvements, resulting a PCE of 11.23% under the warm LED spectrum and 10.70% under the cool LED spectrum. Owing to various optimization steps, the cell performance attains a maximum PCEs of 25.58% and 25% with a relative percentage enhancement of 154.53% and 175.33% compared with the initial cell under LED 200 lx spectra at 2900K and 7500K, respectively. In essence, this study has provided a comprehensive understanding of the interplay between material parameters and device performance in CBTSSe-based solar cells for indoor applications.

Furthermore, CBTSSe offers the advantage of being compatible with cost-effective fabrication techniques, making it a promising candidate for scalable indoor PV applications. As the demand for sustainable energy solutions in indoor environments, such as

smart buildings, wearables, and sensor networks, continues to grow, adaptable bandgap properties of CBTSSe make it an attractive choice for meeting the unique requirements of these applications.

Authors' contribution SQ, AS, and MO wrote the main manuscript text. WZ, MO, MA, and AAAA performed the simulation and prepared the figures. All authors shared in conceptualization, methodology, and validation. All authors reviewed the manuscript.

Data availability Data will be made available on reasonable request.

Declarations

Conflict of interest The authors declare that there is no conflict of interest reported in this paper.

Ethical approval Not Applicable.

References

Ait Abdelkadir, A., Sahal, M., Oublal, E., Kumar, N., Benami, A.: New Sb_2Se_3-based solar cell for achieving high efficiency theoretical modeling. Opt. Quantum Electron. **55**, 514 (2023). https://doi.org/10.1007/s11082-023-04797-7

Chakraborty, R., Sim, K.M., Shrivastava, M., Adarsh, K.V., Chung, D.S., Nag, A.: Colloidal synthesis, optical properties, and hole transport layer applications of Cu_2BaSnS_4 (CBTS) nanocrystals. ACS Appl. Energy Mater. **2**, 3049–3055 (2019). https://doi.org/10.1021/acsaem.9b00473

Cui, X., Sun, K., Huang, J., Lee, C.-Y., Yan, C., Sun, H., Zhang, Y., Liu, F., Hossain, M.A., Zakaria, Y., Wong, L.H., Green, M., Hoex, B., Hao, X.: Enhanced heterojunction interface quality to achieve 93% efficient Cd-free Cu_2ZnSnS_4 solar cells using atomic layer deposition ZnSnO buffer layer. Chem. Mater. **30**, 7860–7871 (2018). https://doi.org/10.1021/acs.chemmater.8b03398

Farooq, W., Alshahrani, T., Kazmi, S.A.A., Iqbal, J., Khan, H.A., Khan, M., Raja, A.A., ur Rehman, A.: Materials optimization for thin-film copper indium gallium selenide (CIGS) solar cell based on distributed braggs reflector. Optik **227**, 165987 (2021). https://doi.org/10.1016/j.ijleo.2020.165987

Gamal, N., Sedky, S.H., Shaker, A., Fedawy, M.: Design of lead-free perovskite solar cell using $Zn_{1-x}Mg_xO$ as ETL: SCAPS device simulation. Optik **242**, 167306 (2021). https://doi.org/10.1016/j.ijleo.2021.167306

Ge, J., Roland, P.J., Koirala, P., Meng, W., Young, J.L., Petersen, R., Deutsch, T.G., Teeter, G., Ellingson, R.J., Collins, R.W., Yan, Y.: Employing overlayers to improve the performance of Cu_2BaSnS_4 Thin film based photoelectrochemical water reduction devices. Chem. Mater. **29**, 916–920 (2017a). https://doi.org/10.1021/acs.chemmater.6b03347

Ge, J., Koirala, P., Grice, C.R., Roland, P.J., Yu, Y., Tan, X., Ellingson, R.J., Collins, R.W., Yan, Y.: Oxygenated CdS buffer layers enabling high open-circuit voltages in earth-abundant Cu_2BaSnS_4 thin-film solar cells. Adv. Energy Mater. **7**, 1601803 (2017b). https://doi.org/10.1002/aenm.201601803

Ghobadi, A., Yousefi, M., Minbashi, M., Kordbacheh, A.H.A., Abdolvahab, A.H., Gorji, N.E.: Simulating the effect of adding BSF layers on $Cu_2BaSnSe_3$ thin film solar cells. Opt. Mater. **107**, 109927 (2020). https://doi.org/10.1016/j.optmat.2020.109927

Gohri, S., Madan, J., Pandey, R., Sharma, R.: Design and analysis of lead-free perovskite-CZTSSe based tandem solar cell. Opt. Quantum Electron. **55**, 171 (2023). https://doi.org/10.1007/s11082-022-04381-5

Green, M., Dunlop, E., Hohl-Ebinger, J., Yoshita, M., Kopidakis, N., Hao, X.: Solar cell efficiency tables (version 57). Prog. Photovolt. Res. Appl. **29**, 3–15 (2021). https://doi.org/10.1002/pip.3371

Green, M.A., Dunlop, E.D., Siefer, G., Yoshita, M., Kopidakis, N., Bothe, K., Hao, X.: Solar cell efficiency tables (Version 61). Prog. Photovolt. Res. Appl. **31**, 3–16 (2023). https://doi.org/10.1002/pip.3506

Hashemi, M., Minbashi, M., Ghorashi, S.M.B., Ghobadi, A.: A modeling study on utilizing low temperature sprayed In_2S_3 as the buffer layer of CuBaSn(S, Se) solar cells. Sci. Rep. **11**, 20038 (2021). https://doi.org/10.1038/s41598-021-99012-6

Henni, W., Rahal, W.L., Rached, D., Boukortt, A.: Effect of introducing Al_2O_3 as a tunnelling layer into p-CBTS/n-CdS heterojunction solar cells. J. Comput. Electron. **22**, 897–905 (2023). https://doi.org/10.1007/s10825-023-02031-x

Huang, X.: Design and development of high performance III-nitrides photovoltaics. PhD dissertation, Arizona State University (2020)

Kumar, A.: Theoretical analysis of CZTS/CZTSSe tandem solar cell. Opt. Quantum Electron. **53**, 528 (2021). https://doi.org/10.1007/s11082-021-03183-5

Minemoto, T., Murata, M.: Theoretical analysis on effect of band offsets in perovskite solar cells. Sol. Energy Mater. Sol. Cells **133**, 8–14 (2015). https://doi.org/10.1016/j.solmat.2014.10.036

Moustafa, M., Al Zoubi, T., Yasin, S.: Numerical analysis of the role of p-$MoSe_2$ interfacial layer in CZTSe thin-film solar cells using SCAPS simulation. Optik **247**, 167885 (2021). https://doi.org/10.1016/j.ijleo.2021.167885

Okil, M., Salem, M.S., Abdolkader, T.M., Shaker, A.: From crystalline to low-cost silicon-based solar cells : a review. Silicon **14**, 1895–1911 (2022). https://doi.org/10.1007/s12633-021-01032-4

Okil, M., Shaker, A., Ahmed, I.S., Abdolkader, T.M., Salem, M.S.: Design and analysis of Sb_2S_3/Si thin film tandem solar cell. Sol. Energy Mater. Sol. Cells **253**, 112210 (2023). https://doi.org/10.1016/j.solmat.2023.112210

Petrović-Ranđelović, M., Kocić, N., Stojanović-Ranđelović, B.: The importance of renewable energy sources for sustainable development. Econ. Sustain. Dev. **4**, 15–24 (2020). https://doi.org/10.5937/esd2002016p

Salah, M.M., Hassan, K.M., Abouelatta, M., Shaker, A.: A comparative study of different ETMs in perovskite solar cell with inorganic copper iodide as HTM. Optik (stuttg). **178**, 958–963 (2019). https://doi.org/10.1016/j.ijleo.2018.10.052

Salem, M.S., Shaker, A., Abouelatta, M., Alanazi, A., Al-Dhlan, K.A., Almurayziq, T.S.: Numerical analysis of hole transport layer-free antimony selenide solar cells: possible routes for efficiency promotion. Opt. Mater. **129**, 112473 (2022a). https://doi.org/10.1016/j.optmat.2022.112473

Salem, M.S., Shaker, A., Almurayziq, T.S., Alshammari, M.T.: Prospective efficiency boosting of full-inorganic single-junction $Sb_2(S, Se)_3$ solar cell. Sol. Energy Mater. Sol. Cells **248**, 112001 (2022b). https://doi.org/10.1016/j.solmat.2022.112001

Scheer, R., Schock, H.W.: Chalcogenide Photovoltaics: Physics, Technologies, and Thin Film Devices. Wiley (2011). https://doi.org/10.1002/9783527633708

Shafi, M.A., Bouich, A., Khan, L., Ullah, H., Guaita, J.M., Ullah, S., Mari, B.: Optimization of electrodeposition time on the properties of Cu_2ZnSnS_4 thin films for thin film solar cell applications. Opt. Quantum Electron. **54**, 533 (2022). https://doi.org/10.1007/s11082-022-03913-3

Shin, D., Saparov, B., Mitzi, D.B.: Defect engineering in multinary earth-abundant chalcogenide photovoltaic materials. Adv. Energy Mater. **7**, 1602366 (2017a). https://doi.org/10.1002/aenm.201602366

Shin, D., Zhu, T., Huang, X., Gunawan, O., Blum, V., Mitzi, D.B.: Earth-abundant chalcogenide photovoltaic devices with over 5% efficiency based on a $Cu_2BaSn(S,Se)_4$ absorber. Adv. Mater. **29**, 1606945 (2017b). https://doi.org/10.1002/adma.201606945

Sun, J.-P., Márquez, J.A., Stange, H., Mainz, R., Mitzi, D.B.: Phase and film formation pathway for vacuum-deposited $Cu_2BaSn(S,Se)_4$ absorber layers. Phys. Rev. Mater. **3**, 55402 (2019)

Tanaka, K., Minemoto, T., Takakura, H.: Analysis of heterointerface recombination by $Zn_{1-x}Mg_xO$ for window layer of Cu(In, Ga)Se_2 solar cells. Sol. Energy **83**, 477–479 (2009). https://doi.org/10.1016/j.solener.2008.09.003

Teymur, B., Levcenco, S., Hempel, H., Bergmann, E., Márquez, J.A., Choubrac, L., Hill, I.G., Unold, T., Mitzi, D.B.: Optoelectronic and material properties of solution-processed earth-abundant $Cu_2BaSn(S, Se)_4$ films for solar cell applications. Nano Energy **80**, 105556 (2021). https://doi.org/10.1016/j.nanoen.2020.105556

Teymur, B., Kim, Y., Huang, J., Sun, K., Hao, X., Mitzi, D.B.: Top stack optimization for $Cu_2BaSn(S,Se)_4$ photovoltaic cell leads to improved device power conversion efficiency beyond 6%. Adv. Energy Mater. **12**, 2201602 (2022). https://doi.org/10.1002/aenm.202201602

Wang, W., Winkler, M.T., Gunawan, O., Gokmen, T., Todorov, T.K., Zhu, Y., Mitzi, D.B.: Device characteristics of CZTSSe thin-film solar cells with 12.6% efficiency. Adv. Energy Mater. **4**, 1301465 (2014). https://doi.org/10.1002/aenm.201301465

Authors and Affiliations

Saif M. H. Qaid[1] · Ahmed Shaker[2] · Mohamed Okil[3] · Muath Alkadi[4] · Abdullah Ahmed Ali Ahmed[5] · Walid Zein[2]

✉ Ahmed Shaker
ahmed.shaker@eng.asu.edu.eg

Saif M. H. Qaid
sqaid@ksu.edu.sa

Mohamed Okil
mohamed.okil@bhit.bu.edu.eg

Muath Alkadi
malkadi@kacst.edu.sa

Abdullah Ahmed Ali Ahmed
abdullah2803@gmail.com

Walid Zein
waleedzein@eng.asu.edu.eg

[1] Department of Physics and Astronomy, College of Sciences, King Saud University, P.O. Box 2455, 11451 Riyadh, Saudi Arabia

[2] Department of Engineering Physics and Mathematics, Faculty of Engineering, Ain Shams University, Cairo, Egypt

[3] Department of Basic Engineering Sciences, Benha Faculty of Engineering, Benha University, Benha, Egypt

[4] King Abdulaziz City for Science and Technology, Riyadh, Saudi Arabia

[5] Center for Hybrid Nanostructures (CHyN) and Fachbereich Physik, Universität Hamburg, 20146 Hamburg, Germany